

Thermally insulating and fire-retardant lightweight anisotropic foams based on nanocellulose and graphene oxide

*Original*

Thermally insulating and fire-retardant lightweight anisotropic foams based on nanocellulose and graphene oxide / Wicklein, B.; Kocjan, A.; Salazar Alvarez, G.; Carosio, Federico; Camino, Giovanni; Antonietti, M.; Bergström, L.. - In: NATURE NANOTECHNOLOGY. - ISSN 1748-3387. - STAMPA. - 10:3(2015), pp. 277-283. [10.1038/nnano.2014.248]

*Availability:*

This version is available at: 11583/2573557 since: 2016-11-28T16:38:10Z

*Publisher:*

Rebecca Walton

*Published*

DOI:10.1038/nnano.2014.248

*Terms of use:*

This article is made available under terms and conditions as specified in the corresponding bibliographic description in the repository

*Publisher copyright*

GENERICO -- per es. Nature : semplice rinvio dal preprint/submitted, o postprint/AAM [ex default]

(Article begins on next page)

## **Thermally insulating and fire-retardant lightweight anisotropic foams based on nanocellulose and graphene oxide**

*Bernd Wicklein, Andraž Kocjan, # German Salazar-Alvarez, Federico Carosio §, Giovanni Camino §, Markus Antonietti ¶, Lennart Bergström\**

Dr. B. Wicklein, Doc. G. Salazar-Alvarez, Prof. L. Bergström

Address line 1:

Department of Materials and Environmental Chemistry

Stockholm University

106 91 Stockholm, Sweden

E-mail: [lennart.bergstrom@mmk.su.se](mailto:lennart.bergstrom@mmk.su.se)

Address line 2:

Wallenberg Wood Science Centre

Royal Institute of Technology, KTH

100 44 Stockholm, Sweden

# Dr. A. Kocjan

Engineering Ceramics Department

Jožef Stefan Institute

1000 Ljubljana, Slovenia

¶ Prof. Markus Antonietti

Max Planck Institute for Colloids and Interfaces

Potsdam-Golm Science Park

Am Mühlenberg 1

14476 Potsdam, Germany

§ Dr. Federico Carosio, Prof. Giovanni Camino

Politecnico di Torino

Corso Duca degli Abruzzi, 24

10129 Torino, Italy

**High-performance thermally insulating materials from renewable resources are needed to improve the energy efficiency of buildings. Traditional fossil-fuel derived insulation materials such as expanded polystyrene (EPS) and polyurethane have a thermal conductivity too high for retrofitting and building new passive houses without severely compromising the architectural design. Tailored superinsulating materials such as aerogels and vacuum insulating panels are fragile and susceptible to perforation. Here, we show that freeze-casting suspensions of cellulose nanofibres, graphene oxide and sepiolite nanorods produces super-insulating, fire-retardant and strong anisotropic foams that perform better than traditional polymer-based insulating materials. The foams are ultralight, show excellent combustion resistance and exhibit a thermal conductivity of  $15\text{mW m}^{-1} \text{K}^{-1}$ , which is about half that of EPS. At  $30\text{ }^\circ\text{C}$  and 85% relative humidity, the foams retained more than half of their initial strength. Our results show that nanoscale engineering is a promising strategy for producing foams with excellent properties using cellulose and other renewable and abundant nanosized fibrous materials.**

The energy needed to maintain a pleasant interior atmosphere accounts for more than 10 % of the world's total energy consumption.<sup>1</sup> Thermal insulation plays a major role in controlling the energy efficiency of buildings and there is a need to substantially reduce the thermal conductivity,  $\lambda$ , compared to the currently used insulation materials; e.g. EPS ( $\lambda=30\text{-}40\text{ mW m}^{-1} \text{K}^{-1}$ ), polyurethane ( $\lambda=20\text{-}30\text{ mW m}^{-1} \text{K}^{-1}$ ), fibreglass ( $\lambda=33\text{-}44\text{ mW m}^{-1} \text{K}^{-1}$ ), and mineral wool ( $\lambda=30\text{-}40\text{ mW m}^{-1} \text{K}^{-1}$ ).<sup>2</sup> In fact, reducing the thermal conductivity significantly below the value for air ( $\lambda=25\text{ mW m}^{-1} \text{K}^{-1}$ ) is needed to minimize the required space and materials while permitting retrofitting of older buildings without severely compromising the architectural design. Approaches to obtain super-insulating materials include the replacement of air with another gas or vacuum<sup>3,4</sup> or by reducing the pore size below the mean free path of air.<sup>2</sup> However, maintaining a special gas or vacuum inside insulating panels for extended time is challenging, which can result in a loss of the initially low thermal conductivity with time.<sup>2</sup> Nanoporous insulating materials such as silica aerogels can be used under ambient conditions and still maintain a low  $\lambda$  of about  $17\text{-}21\text{ mW m}^{-1} \text{K}^{-1}$  but they are brittle and difficult to prepare in large sizes.<sup>5</sup>

Renewable, biopolymer-based materials such as wood chips, recycled paper and cork<sup>2</sup> were extensively used for thermal insulation prior to the introduction of fossil fuel-based foams but their insulating performance is relatively poor with thermal conductivities of 40-50 mW m<sup>-1</sup>K<sup>-1</sup>. However, with the emergence of nanocellulose extracted from wood and other sources<sup>6</sup> there are now possibilities for nanoscale engineering<sup>7,8</sup> of renewable materials to generate more efficient thermal insulators.<sup>9</sup> Importantly, previous work has shown that the use of nanosized 1- and 2-dimensional materials such as carbon nanotubes, silicon and silicate nanorods, exfoliated clays, and SiGe nanolaminates<sup>10,11,12</sup> can substantially reduce the solid heat conduction by the creation of phonon barriers.<sup>13,14</sup>

A challenge, however, for biopolymer-based insulation materials is their poor resistance to fire and their moisture sensitivity. Recent work has shown that nanomaterials like clays and graphenoids can provide a good fire retardancy and excellent mechanical properties to organic polymer-based nanocomposites.<sup>15,16,17</sup> Different strategies have been used to improve the moisture sensitivity of cellulose-based materials including e.g.: crosslinking, polyelectrolyte multilayers and hydrophobisation.<sup>8,18,19</sup>

In this work, we describe lightweight (7.5 kg m<sup>-3</sup>), highly porous foams that are produced by freeze-casting<sup>20</sup> colloidal suspensions of cellulose nanofibres (CNF) and graphene oxide (GO), together with sepiolite nanorods (SEP) (**Figure 1a, 1b**). The anisotropic nanocomposite foams are mechanically stiff in the freezing direction and able to sustain a considerable load (**Figure 1c**). The thermal conductivity of the nanocomposite foams is sufficiently low to allow for a more than 50% reduction of the passive house standards insulation thickness compared with commercial EPS (**Figure 1d**) and the nanocomposite foams also show a high fire-resistance (**Figure 1e**).

### **Fabrication and structural features of nanocomposite foams**

Freeze-casting was performed by controlled freezing of an aqueous suspension of CNF, GO, and SEP in a mould that is placed on top of a cold finger that is immersed in a liquid nitrogen bath (**Figure 1a**). Freeze-casting offers a versatile approach to produce highly anisotropic porous materials<sup>20</sup> where ice crystals grow with the temperature gradient and eventually result in a frozen material consisting of anisotropic ice crystals surrounded by walls of the dispersed nanoparticles (**Figure**



**1a).** Freeze-casting has been used to prepare porous scaffolds and bioceramics<sup>20,21</sup> and recent work also includes attempts to produce thermally insulating ceramics.<sup>22</sup> Adjustments of the freezing conditions provide high control over pore orientation, size and density and we found that higher cooling rates result in smaller pore diameters (cell sizes) (**Supplementary Figure 1**). We have produced freeze-cast, lightweight nanocellulose-based nanocomposite foams (**Figure 1b, Supplementary Figure 2**) using a high cooling rate of 15 K min<sup>-1</sup>, where small macropores with a relatively narrow pore size distribution were obtained.

Microstructural analysis by a combination of scanning electron microscopy (SEM) and X-ray microtomography of the nanocomposite foams reveal aligned tubular pores (**Figure 2a-c**) The pores have a diameter of about 20  $\mu\text{m}$  and a cell wall thickness of 0.2-0.4  $\mu\text{m}$  (**Figure 2a**). The freeze-cast foams have a density of 5.6 kg m<sup>-3</sup> and 7.5 kg m<sup>-3</sup> for pure CNF and CNF-GO-BA-SEP nanocomposite foams, respectively (**Table 1 and Supplementary Table 1**), that is similar or slightly lower than previously reported open-cell CNF foams (15 kg m<sup>-3</sup>)<sup>23</sup> and CNF aerogels (7-20 kg m<sup>-3</sup>).<sup>24,25</sup>

X-ray microtomography unveils that the pores run as millimeter-long tubes parallel to the freezing direction throughout the material (**Figure 2b,c**). Cross-sections obtained at different positions along the ice growth direction (**Figure 2d,e**) show that the 2-dimensional pore density decreases by only 30 % from the bottom to the top of the foam. This suggests that the pore structure is uniform and that the nanocomposite foams have a relatively moderate extent of pore interconnectivity. High-resolution (HR)-SEM shows that the cell walls of the nanocomposite foams are thin and smooth and resemble sheets of nanopaper wrapped around the tubular pores (**Figure 2f**). The SEP nanorods are homogeneously distributed within the cell wall and no aggregates of CNF or GO can be observed, suggesting that the process generates foam walls with a high degree of homogeneity.

### Thermal transport properties

**Figure 3a** illustrates the convection ( $\lambda_{\text{conv}}$ ), conduction (with  $\lambda_{\text{g}}$  representing gas conduction and  $\lambda_{\text{sol}}$  representing solid conduction) and radiation ( $\lambda_{\text{rad}}$ ) contributions to the thermal conductivity of the freeze-cast foams. **Figure 3b** shows that the thermal conductivity in the radial orientation (normal to the tubular pores) of

CNF foams is as low as  $18 \text{ mW m}^{-1} \text{ K}^{-1}$ , and that the addition of 10 wt% graphene oxide and 10 wt% sepiolite to produce a nanocomposite foam reduces  $\lambda$  to  $15 \text{ mW m}^{-1} \text{ K}^{-1}$ . The ability of the nanocellulose-based foams to yield a  $\lambda$  value significantly below the value of air and less than half the value for fossil fuel-based insulating materials like EPS can be related to thermal properties of the nanosized components and the microstructure in the cell walls. Analysis of nitrogen gas adsorption isotherms shows that the cell walls are mesoporous with a 20 % porosity and an average pore size of 3 nm (**Supplementary Figure 3**). The gas conduction  $\lambda_g$  within the walls can be estimated according to

$$\lambda_g = \frac{\lambda_{g0}\Pi}{1+2\beta Kn} \quad (1)$$

where  $\Pi$  denotes the porosity,  $\lambda_{g0}$  is the gaseous conductivity in free space ( $25 \text{ mW m}^{-1} \text{ K}^{-1}$ ),  $\beta \approx 2$  for air in aerogels, and  $Kn$  is the Knudsen number

$$Kn = \frac{l_m}{\delta} \quad (2)$$

which relates the mean free path  $l_m$  of a gas molecule to the pore diameter  $\delta$ . We estimate that  $l_m$  in the nanocomposite foam walls is only 10 nm versus 75 nm in free space, which dramatically reduce the gaseous conductivity to below  $1 \text{ mW m}^{-1} \text{ K}^{-1}$ .<sup>26</sup> The use of nanosized components (CNF, GO and SEP) may also infer a significant interfacial thermal resistance,<sup>10</sup> so-called Kapitza resistance  $R_k$ ,<sup>27</sup> which reduces the (solid) conduction of the walls. The solid conduction of the cell wall can be estimated by a weighted average of the effective solid conduction values  $\lambda_{sol}^*$  of the individual components of the nanocomposite foam by using

$$\lambda_{sol}^* = \frac{\lambda_{sol}}{1+\lambda_{sol}\frac{R_k}{d}} \quad (3)$$

where  $d$  is the particle size and  $\lambda_{sol}$  is the solid conduction of the individual components. The  $R_k$  values of the various components of the CNF-GO-BA-SEP nanocomposite foam were taken from literature including a  $R_k$  value for CNF assumed to be similar in magnitude to carbon nanotubes ( $10^{-7} \text{ m}^2 \text{ K W}^{-1}$ )<sup>28</sup> (**Supplementary Table 2**). Estimates using Eq. 3 (see **Supplementary section** for detailed description) suggest that phonon scattering effects can reduce  $\lambda_{sol}$  in the walls from around  $1000 \text{ mW m}^{-1} \text{ K}^{-1}$  for a bulk material with a composition identical to the nanocomposite foam to below  $40 \text{ mW m}^{-1} \text{ K}^{-1}$  for the nanostructured composite foam wall. The convection in the radial direction should be insignificant considering that the small pore size is well below the onset of natural convection<sup>29</sup> and that the

inter-connectivity of the tubular pores is small, as inferred from the X-ray microtomography data (**Figure 2 d,e**).

Carbonaceous materials are known to be efficient IR absorbers<sup>30,31</sup> and are frequently used to reduce the radiative contribution in insulating materials. IR-measurements showed that addition of 10 % of GO increases the mass attenuation coefficient ( $\mu/\rho$ ) in the mid-IR range by 26 % compared to pure CNF foams (**Supplementary Table 3**). **Figure 3b** shows that the apparent thermal conductivity in the axial direction (along the pores) is significantly higher than in the radial direction. This strong orientation effect is clearly a consequence of the anisotropic pore and wall structure and related to a combination of orientation-dependent radiation<sup>29</sup> and solid conduction in the walls as well as possibly natural convection in axial direction.<sup>32</sup> Thermographic recordings (**Figure 3c,d**) illustrate the efficient thermal insulation in the radial direction of the nanocomposite foams compared to EPS. The thermal conductivity in the radial direction of nanocomposite foams with the same composition but prepared by freeze-casting at cooling rates from 1 to 15 K min<sup>-1</sup> (**Supplementary Figure 1**), is nearly identical although the cell size varies from 150 to 20  $\mu\text{m}$ , respectively. This supports the conjecture that the radial thermal transport properties of the nanocomposite foams are primarily controlled by the composition and microstructure of the pore walls.

### **Mechanical strength**

The stress-strain measurements (**Figure 4a**) display the typical deformation behaviour of an open honeycomb-like foam, i.e. a linear elastic behaviour at low strain followed by a cell collapse related stress reduction at intermediate strains, and finally a plastic yielding plateau with subsequent stiffening at high strain.<sup>33</sup> We obtain a Young's modulus  $E=570$  kPa along the pore (freezing) direction (**Figure 4b**). In fact, the CNF-GO-BA-SEP foam has a specific Young's modulus  $E_S=77$  kNm kg<sup>-1</sup>, which is significantly higher than previously reported nanocellulose foams<sup>15</sup> or silica aerogels (5-20 kNm kg<sup>-1</sup>)<sup>5,34</sup> and is in the range of EPS and EPU foams (10-100 kNm kg<sup>-1</sup>).<sup>33</sup> The high modulus is related to the extraordinary high moduli of nanocellulose and graphene oxide and that boric acid (BA) makes the cell walls stiffer by crosslinking (**Figure 4b**). The appearance of a carbonyl band at 1720 cm<sup>-1</sup> (**Figure 4c and Supplementary Figure 4**), suggests that borate esters and anhydrides form in both the CNF and the CNF-GO nanocomposite foams. Indeed, previous work has

shown that boric acid can form borate ester bonds with hydroxyl moieties on GO nanosheets, resulting in an increase of the stiffness of GO nanopaper by 255 %.<sup>35</sup> Covalent borate ester bonds between hydroxymethyl groups on cellulose fibrils are also frequently found in plants contributing to the high strength of cell walls.<sup>36</sup>

We have also investigated how the mechanical properties are affected when the nanocomposite foams are subjected to an elevated relative humidity (rh) and temperature. The modulus of the nanocomposite foams decrease from 530 to 300 kPa when the atmosphere is changed from 50 %rh and 23 °C to 85 %rh and 30 °C, respectively (**Figure 4d**). This decrease in mechanical properties at high rh is relatively modest considering previous reports on moisture-induced reduction by up to one order of magnitude of the stiffness and strength of nanocellulose-based materials such as nanopaper<sup>37</sup> or aerogels.<sup>38</sup> In fact, the specific modulus of the CNF-nanocomposite foams at 85 %rh and 30 °C is 38 kNm kg<sup>-1</sup>, which is higher than dry silica aerogels and similar to flexible PU foams. The moisture sensitivity of cellulose-based materials is generally attributed to a weakening of interfibrillar bonding. The covalent nature of the borate crosslinking is likely to be responsible for preserving the structural integrity and mechanical strength of the nanocomposite foams in moist conditions.

The elastic properties of the nanocomposite foam partially recover (390 kPa) after repose for one day at 50 %rh and 23 °C (**Figure 4d**), suggesting that the exposure to high humidity results in a relatively small degree of permanent network disintegration. This is promising and indicates that the ultralight nanocomposite foams could display a high degree of breathability, similar to traditional cellulose-based insulating materials like dry (loose fill) cellulose.

### **Fire retardancy**

Petroleum-based polymeric insulation materials are easily ignitable, requiring the addition of flame retardants.<sup>15,39</sup> Unfortunately, many of the commonly used flame retardants are halogenated or phosphorous compounds with negative environmental and health impact<sup>40,41</sup> but recent work has shown that the fire retardancy of organic-inorganic composites can be significantly improved with the addition of well-distributed inorganic filler such as clays and also graphenoids.<sup>15,16</sup> Vertical burning tests (UL 94) show that nanocellulose-based composite foams with an optimized

addition of GO (10 wt.%), SEP (10 wt.%) and BA (3 wt.%) display a very good fire retardancy where the flame does not self-propagate (**Figure 5a**). Foams with suboptimal composition, i.e. with no GO or low clay content display some fire retardancy but shrink much more than the nanocomposite foams with an optimal composition (**Supplementary Videos 1**). Thermogravimetric analysis (TGA) in air reveals that the thermo-oxidative stability of the CNF foams increases by the stepwise addition of GO, BA, and SEP (**Supplementary Figure 5**). Nanocomposite foams with the optimized composition (10/10/3 wt% of GO, SEP and BA, respectively) yield a carbon-rich final residue of 55 wt% that is stable up to 900 °C. For the optimal foam composition, the limiting oxygen index (LOI), which gives the oxygen concentration (in %) needed to keep a material burning, is as high as 34 (**Supplementary Videos 2**), which is 60 % higher than the O<sub>2</sub> level (21 %) in air. In fact, the nanocomposites have a significantly higher LOI-value compared to commercial, flame retardant-containing polymer-based foams, which display typical LOI-values between 22 and 25.<sup>42</sup>

In addition, the fire retardant behaviour was further assessed with oxygen consumption cone calorimetry which relate to developing fire scenarios. Foams were exposed to a defined heat flux of 35 kW m<sup>-2</sup> and we found that while CNF foams always ignite, CNF-GO-BA-SEP nanocomposite foams are on the borderline between only smouldering and ignition (**Figure 5b**) which stands in contrast to even halogenated PU foams<sup>42</sup> or layer-by-layer modified polymer foams<sup>43</sup> that always ignite under similar conditions. Estimates of the peak of heat release rates (pkHRR) have also been obtained and although the values are small due to the limited amount of material, we find that the nanocomposite foams display a pkHRR that is 25% lower than the CNF foams (**Figure 5b, Supplementary Figure 6**).

Our results (**Figure 5c**) show that the intensity ratio of the D and G Raman bands of GO in the nanocomposite at 1360 and 1610 cm<sup>-1</sup>, respectively, decreases significantly after burning. This can be attributed to a reduction of GO to graphene in the flame<sup>44,45</sup> and transformation of the carbon sources (i.e. GO and CNF) into char.<sup>46</sup> Indeed, analysis of the chemical transformations of CNF foams shows that boric acid acts as char former<sup>47</sup> and facilitates the graphitization of CNF<sup>48</sup> (see Raman spectra in **Supplementary Figure 7**) corroborating previous studies on the flame retardant properties of GO and boric acid.<sup>46,47</sup> **Figure 5d** shows that sepiolite may form a protective silicate-rich surface layer upon burning, similar to intumescent

clay-polymer nanocomposites<sup>49</sup> as indicated by the intense silicate bands at 1104, 932, and 859  $\text{cm}^{-1}$ .

## Conclusions

In summary, we have shown that anisotropic, nanoporous composite foams formed by nanocellulose, graphene oxide, and sepiolite display a combination of very low radial thermal conductivity ( $15 \text{ mW m}^{-1} \text{ K}^{-1}$ ), high axial specific Young's modulus ( $77 \text{ kNm kg}^{-1}$ ), and good fire retardancy (LOI of 34 and only occasional ignition in cone calorimetry tests). The thermal conductivity of the freeze-cast nanocomposite foams is substantially lower than traditional insulation materials such as EPS and polyurethane. The addition of graphene oxide and sepiolite to naturally abundant nanocellulose crosslinked with boric acid results in a higher specific mechanical strength in the axial direction than silica aerogels and also provide the nanocomposite foams with a good moisture resistance. The specific modulus of the nanocomposite foams subjected to 85% rh and 30 °C is  $38 \text{ kNm kg}^{-1}$ , which is higher than dry silica aerogels and similar to flexible PU foams.

The anisotropic thermal and mechanical properties of the freeze-cast nanocomposite foams are suitable for applications such as thermal insulation of walls where the high strength in the axial direction and a low thermal conductivity in the radial direction can be fully utilised.

All the components contribute to protecting the nanocellulose from self-igniting and results in a flame-retardant material with a significantly higher LOI-value and better combustion resistance than polymer foams that contain halogenated flame retardants. Our results provide substantial motivation to continue the development of high-performance thermal insulating materials based on renewable or widely abundant resources for the improvement of energy efficiency and reduction of the environmental impact of buildings.

## Methods

**Nanocellulose suspension.** CNF was obtained from a defibrillation process of soft wood pulp.<sup>50</sup> In brief, an aqueous suspension of pulp from Norwegian spruce was subjected to an enzymatic pre-treatment to liberate wood fibres followed by a TEMPO-mediated oxidation step to render carboxylated fibres (600 mmol g<sup>-1</sup> charge). Subsequent mechanical disintegration using a high-pressure homogenizer equipped with a 100 µm chamber renders fully defibrillated cellulose nanofibrils. The mechanical treatment results in a highly viscous CNF dispersion with a concentration of about 1 wt.%. The CNF are long and flexible fibres with a thickness of 5 nm and 1-2 µm in length (**Supplementary Figure 8**).

**Graphene oxide, sepiolite and boric acid.** GO produced from natural graphite was obtained as exfoliated powder from JCNano Inc., Nanjing, China (**Supplementary Figure 8**), and dispersed in Milli-Q<sup>®</sup> water adjusting the final pH to 7. Sepiolite clay (SEP) is a rod-like microporous magnesiosilicate that is 25 nm thick and 1 µm long (**Supplementary Figure 8**) was purchased from Aldrich and used as is. Boric acid (BA) was purchased from Aldrich and used as is.

**Processing.** Aqueous suspensions of CNF (adjusted to pH 7) with a concentration of 5 mg ml<sup>-1</sup> were mixed with 5-10 wt.% GO, 5-15 wt.% SEP and 1-3 wt.% BA (with respect to CNF dry mass) using a high-speed disperser (Ultra-Turrax, IKA, Germany). The colloidally stable composite suspensions were degassed and kept under slow stirring prior to freeze-casting using a custom built freeze-caster (**Supplementary Figure 9**). The composite suspensions were poured into cylindrical or rectangular teflon moulds that sit on a copper rod in contact with a liquid N<sub>2</sub> bath. The cooling rate of the suspension can be controlled by thermocouples and electrical heating elements inserted in the copper rod. The suspensions were frozen at cooling rates of 1-15 K min<sup>-1</sup> followed by freeze drying (Hetosicc, Heto Lab, Denmark).

**Characterization.** The starting materials CNF, GO and SEP were characterized using a scanning electron microscope (SEM, JEOL JSM-7001F) and a transmission electron microscope (TEM, JEOL JEM-2100 LaB6). The foams were analysed by IR spectroscopy (Varian 670-IR spectrometer and 610-IR microscope), Raman spectroscopy (LabRAM HR 800, Horiba), SEM (Hitachi TM3000), and micro-tomography (Xradia MicroXCT-200). Apparent densities were calculated by weighing

the foams and measuring their volumes. The diameters of the tubular pores size and the pore densities were estimated from analysis of SEM cross-section images using the ImageJ 1.45s software. The specific surface area and porosity of the cell walls was determined from N<sub>2</sub> adsorption isotherms (ASAP2020 instrument, Micromeritics Instrument Corporation).

**Thermal, flame-retardant and mechanical properties.** The thermal transport properties were assessed with a Hot Disk TPS 2500 S instrument (Hot-disk AB, Sweden) using 20 mW input power in the transient mode. A 6.4 mm Ni wire sensor was used and the samples were probed in the anisotropic mode to simultaneously obtain information on the thermal conductivity and diffusivity. The data was obtained from 5 independent measurements of 4 replicas. The specific heat capacity of the foams was determined with the hot-disk instrument (see **Supplementary Figure 10**). Thermographic images were captured using an IR thermal camera (Fluke Ti55FT IR FlexCam) with a thermal sensitivity of  $\leq 0.05$  °C. For this purpose the samples were mounted on stage made of mullite fibre wool and the heating source was a small copper cylinder. The flame retardancy behaviour was assessed by UL94 standardized vertical burning tests, the limiting oxygen index using the ASTM D2863 method and by thermogravimetric analysis in technical air with a heating rate of 10 K min<sup>-1</sup> (PerkinElmer TGA 7). The combustion behaviour of squared samples (50x50x10 mm<sup>3</sup>) has been investigated by cone calorimetry (Fire Testing Technology, FTT) under a heat flux of 35 kW m<sup>-2</sup> in a horizontal configuration. Prior to the tests, all specimens were conditioned for 24 h at 23 °C and 50 %rh in a climate chamber. Four specimen of each type of sample were measured in order to ensure reproducible and significant data. The mechanical properties of the foams were measured on an Instron 5944 instrument using 50 and 500 N load cells. The samples were always tested under controlled conditions (23 °C and 50 % relative humidity). For the assessment of the mechanical behaviour under high relative humidity, the foams were exposed to 85 %rh at 30 °C for 6 days in a climate chamber (KBF 115, Binder). The number of replicas for all mechanical tests was four.



## References

1. International Energy Agency. *Technology roadmap: Energy efficient building envelopes*. (2013).
2. Jelle, B.P. Traditional, state-of-the-art and future thermal building insulation materials and solutions – Properties, requirements and possibilities. *Energy Build.* **43**, 2549–2563 (2011).
3. Fernández, J.E. Materials for aesthetic, energy-efficient, and self-diagnostic buildings. *Science* **315**, 1807–1810 (2007).
4. Alam, M., Singh, H. & Limbachiya, M.C. Vacuum Insulation Panels (VIPs) for building construction industry – A review of the contemporary developments and future directions. *Appl. Energy* **88**, 3592–3602 (2011).
5. Hüsing, N. & Schubert, U. Aerogels - Airy Materials: Chemistry, Structure, and Properties. *Angew. Chemie Int. Ed.* **37**, 22–45 (1998).
6. Moon, R.J., Martini, A., Nairn, J., Simonsen, J. & Youngblood, J. Cellulose nanomaterials review: structure, properties and nanocomposites. *Chem. Soc. Rev.* **40**, 3941–94 (2011).
7. Olsson, R.T. *et al.* Making flexible magnetic aerogels and stiff magnetic nanopaper using cellulose nanofibrils as templates. *Nature Nanotech.* **5**, 584–588 (2010).
8. Hamedi, M. *et al.* Nanocellulose aerogels functionalized by rapid layer-by-layer assembly for high charge storage and beyond. *Angew. Chemie (Int.ed.)* **52**, 12038–12042 (2013).
9. Kobayashi, Y., Saito, T. & Isogai, A. Aerogels with 3D ordered nanofiber skeletons of liquid-crystalline nanocellulose derivatives as tough and transparent insulators. *Angew. Chemie (Int. ed.)* (2014) doi:10.1002/anie.201405123.
10. Pernot, G. *et al.* Precise control of thermal conductivity at the nanoscale through individual phonon-scattering barriers. *Nature Mater.* **9**, 491–495 (2010).
11. Huxtable, S.T. *et al.* Interfacial heat flow in carbon nanotube suspensions. *Nature Mater.* **2**, 731–734 (2003).
12. Losego, M.D., Blitz, I.P., Vaia, R.A, Cahill, D.G. & Braun, P.V. Ultralow thermal conductivity in organoclay nanolaminates synthesized via simple self-assembly. *Nano Lett.* **13**, 2215–2219 (2013).
13. Yu, J.-K., Mitrovic, S., Tham, D., Varghese, J. & Heath, J.R. Reduction of thermal conductivity in phononic nanomesh structures. *Nature Nanotech.* **5**, 718–721 (2010).

14. Losego, M.D., Grady, M.E., Sottos, N.R., Cahill, D.G. & Braun, P.V. Effects of chemical bonding on heat transport across interfaces. *Nature Mater.* **11**, 502–506 (2012).
15. Kashiwagi, T. *et al.* Nanoparticle networks reduce the flammability of polymer nanocomposites. *Nature Mater.* **4**, 928–933 (2005).
16. Li, Y. *et al.* Flame retardant behavior of polyelectrolyte-clay thin film. *ACS Nano* **4**, 3325–3337 (2010).
17. Wagner, H.D. Nanocomposites: Paving the way to stronger materials. *Nature Nanotech.* **2**, 742–744 (2007).
18. Lingström, R., Notley, S.M. & Wågberg, L. Wettability changes in the formation of polymeric multilayers on cellulose fibres and their influence on wet adhesion. *J. Colloid Interface Sci.* **314**, 1–9 (2007).
19. Jin, C., Jiang, Y., Niu, T. & Huang, J. Cellulose-based material with amphiphobicity to inhibit bacterial adhesion by surface modification. *J. Mater. Chem.* **22**, 12562–12567 (2012).
20. Deville, S., Saiz, E., Nalla, R.K. & Tomsia, A.P. Freezing as a path to build complex composites. *Science* **311**, 515–518 (2006).
21. Gutiérrez, M., Ferrer, M. & Monte, F. del. Templated Materials: Sophisticated Structures Exhibiting Enhanced Functionalities Obtained after Unidirectional Freezing and Ice-Segregation-Induced Self-Assembly. *Chem. Mater.* **20**, 634–648 (2008).
22. Hong, C.-Q., Han, J.-C., Zhang, X.-H. & Du, J.-C. Novel nanoporous silica aerogel impregnated highly porous ceramics with low thermal conductivity and enhanced mechanical properties. *Scr. Mater.* **68**, 599–602 (2013).
23. Ali, Z.M. & Gibson, L.J. The structure and mechanics of nanofibrillar cellulose foams. *Soft Matter* **9**, 1580–1588 (2013).
24. Svagan, A.J., Samir, M.A.S.A. & Berglund, L.A. Biomimetic foams of high mechanical performance based on nanostructured cell walls reinforced by native cellulose nanofibrils. *Adv. Mater.* **20**, 1263–1269 (2008).
25. Jiang, F. & Hsieh, Y.-L. Super water absorbing and shape memory nanocellulose aerogels from TEMPO-oxidized cellulose nanofibrils via cyclic freezing–thawing. *J. Mater. Chem. A* **2**, 350–359 (2014).
26. Lu, X., Arduini-Schuster, M., Kuhn, J. & Nilsson, O. Thermal conductivity of monolithic organic aerogels. *Science* **469**, 1990–1991 (1992).
27. Kapitza, P.L. The study of heat transfer in helium II. *J. Phys.* **4**, 181–210 (1941).

28. Han, Z. & Fina, A. Thermal conductivity of carbon nanotubes and their polymer nanocomposites: A review. *Prog. Polym. Sci.* **36**, 914–944 (2011).
29. Glicksman, L.R. in *Low density cellular plastics* (Hilyard, N.C., Cunningham, A. & Glicksman, L.R.) 104–152 (Springer Netherlands, 1994).
30. Acik, M. *et al.* Unusual infrared-absorption mechanism in thermally reduced graphene oxide. *Nature Mater.* **9**, 840–845 (2010).
31. Balandin, A.A. Thermal properties of graphene and nanostructured carbon materials. *Nature Mater.* **10**, 569–581 (2011).
32. Antunes, M. *et al.* Thermal conductivity anisotropy in polypropylene foams prepared by supercritical CO<sub>2</sub> dissolution. *Mater. Chem. Phys.* **136**, 268–276 (2012).
33. Gibson, L.J. & Ashby, M.F. *Cellular solids: Structure and properties*. (Cambridge University Press, 1999).
34. Obrey, K. A. D., Wilson, K. V. & Loy, D. A. Enhancing mechanical properties of silica aerogels. *J. Non. Cryst. Solids* **357**, 3435–3441 (2011).
35. An, Z., Compton, O.C., Putz, K.W., Brinson, L.C. & Nguyen, S.T. Bio-inspired borate cross-linking in ultra-stiff graphene oxide thin films. *Adv. Mater.* **23**, 3842–3846 (2011).
36. Pappin, B., Kiefel, M.J. & Houston, T.A. in *Carbohydrates - Comprehensive studies on glycobiology and glycotechnology*. 37–54 (Intech, 2012).
37. Benítez, A., Torres-Rendon, J., Mikko Poutanen & Walther, A. Humidity and multiscale structure govern mechanical properties and deformation modes in films of native cellulose nanofibrils. *Biomacromolecules* **14**, 4497–4506 (2013).
38. Bénézet, J.-C., Stanojlovic-Davidovic, A., Bergeret, A., Ferry, L. & Crespy, A. Mechanical and physical properties of expanded starch, reinforced by natural fibres. *Ind. Crops Prod.* **37**, 435–440 (2012).
39. Dasari, A., Yu, Z.-Z., Cai, G.-P. & Mai, Y.-W. Recent developments in the fire retardancy of polymeric materials. *Prog. Polym. Sci.* **38**, 1357–1387 (2013).
40. Hale, R.C. *et al.* Flame retardants: Persistent pollutants in land-applied sludges. *Nature* **412**, 140–141 (2001).
41. Shaw, S.D. *et al.* Halogenated flame retardants: do the fire safety benefits justify the risks? *Rev. Environ. Health* **25**, 261–305 (2010).
42. Singh, H. & Jain, A. Ignition, combustion, toxicity, and fire retardancy of polyurethane foams: A comprehensive review. *J. Appl. Polym. Sci.* **111**, 1115–1143 (2009).

43. Carosio, F., Di Blasio, A., Cuttica, F., Alongi, J. & Malucelli, G. Self-assembled hybrid nanoarchitectures deposited on poly(urethane) foams capable of chemically adapting to extreme heat. *RSC Adv.* **4**, 16674–16680 (2014).
44. Shi, Y. & Li, L.-J. Chemically modified graphene: Flame retardant or fuel for combustion? *J. Mater. Chem.* **21**, 3277–3279 (2011).
45. Dreyer, D.R., Park, S., Bielawski, C.W. & Ruoff, R.S. The chemistry of graphene oxide. *Chem. Soc. Rev.* **39**, 228–240 (2010).
46. Higginbotham, A.L., Lomeda, J.R., Morgan, A.B. & Tour, J.M. Graphite oxide flame-retardant polymer nanocomposites. *ACS Appl. Mater. Interfaces* **1**, 2256–2261 (2009).
47. Lu, S.-Y. & Hamerton, I. Recent developments in the chemistry of halogen-free flame retardant polymers. *Prog. Polym. Sci.* **27**, 1661–1712 (2002).
48. Byrne, G.A., Gardiner, D. & Holmes, F.H. The pyrolysis of cellulose and the action of flame-retardants. *J. Appl. Chem.* **16**, 81–88 (1966).
49. Fina, A., Bocchini, S. & Camino, G. in *Fire Polym. V* **1013**, 10–24 (American Chemical Society, 2009).
50. Wågberg, L. *et al.* The build-up of polyelectrolyte multilayers of microfibrillated cellulose and cationic polyelectrolytes. *Langmuir* **24**, 784–795 (2008).

**Figures:**

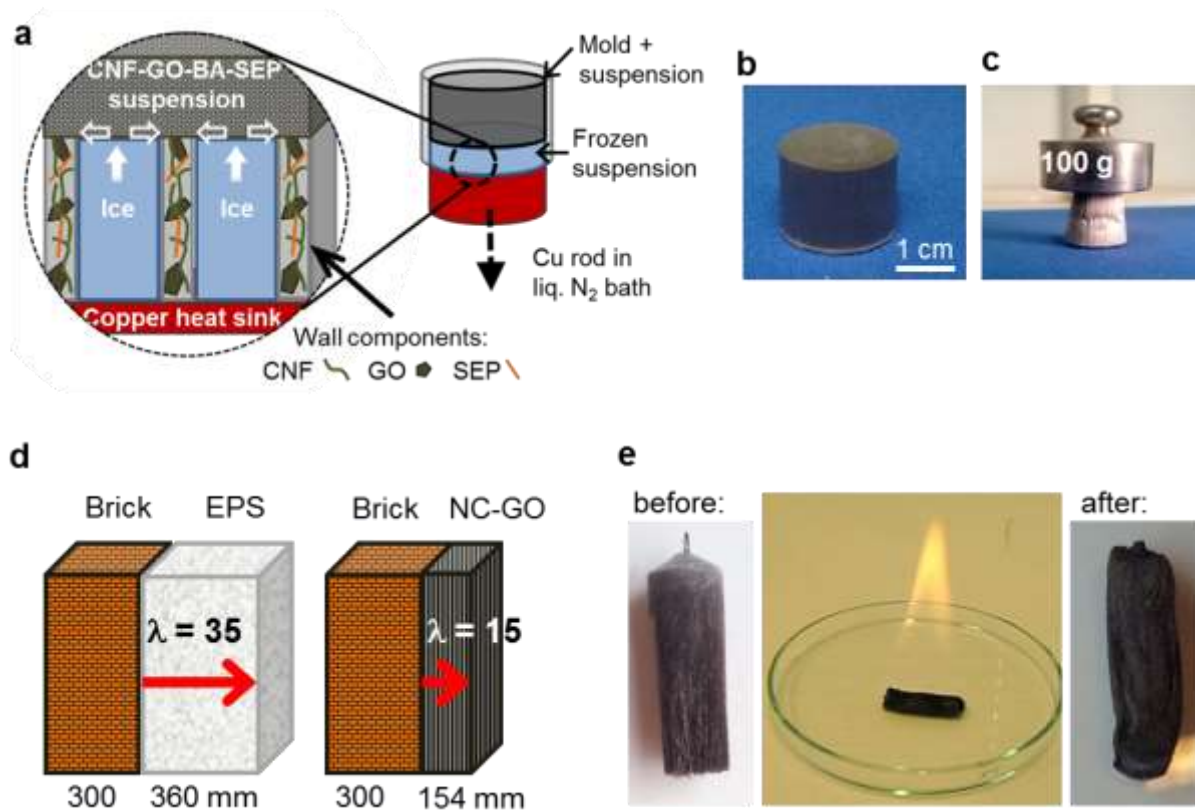


**Figure 1. Fabrication and overview of the mechanical, thermal and fire retardant**

**properties of nanocomposite foams.** **a)** Illustration of freeze-casting process highlighting the growth of anisotropic ice crystals surrounded by walls of the dispersed nanoparticles (not drawn to scale). **b)** Photograph of the 77 % CNF-10 % GO-10 % SEP-3 % BA nanocomposite foam. **c)** CNF-GO-BA-SEP based composite foam with a density of  $7 \text{ kg m}^{-3}$  can sustain a 100 g weight. **d)** Schematic illustration of the thickness of EPS and an optimized nanocomposite foam needed for passive house insulation (energy loss  $\leq 100 \text{ mW m}^{-2} \text{ K}^{-1}$ ). The thicknesses of the brick and the insulating layers are given in mm and calculated using  $\lambda$  values of  $35 \text{ mW m}^{-1} \text{ K}^{-1}$  and  $15 \text{ mW m}^{-1} \text{ K}^{-1}$  for EPS and the nanocellulose(NC)-based composite foam, respectively. **e)** Burning an ethanol-soaked nanocomposite foam of the same composition as in Figure 1b results in a carbonised residue with a similar shape as the original material.

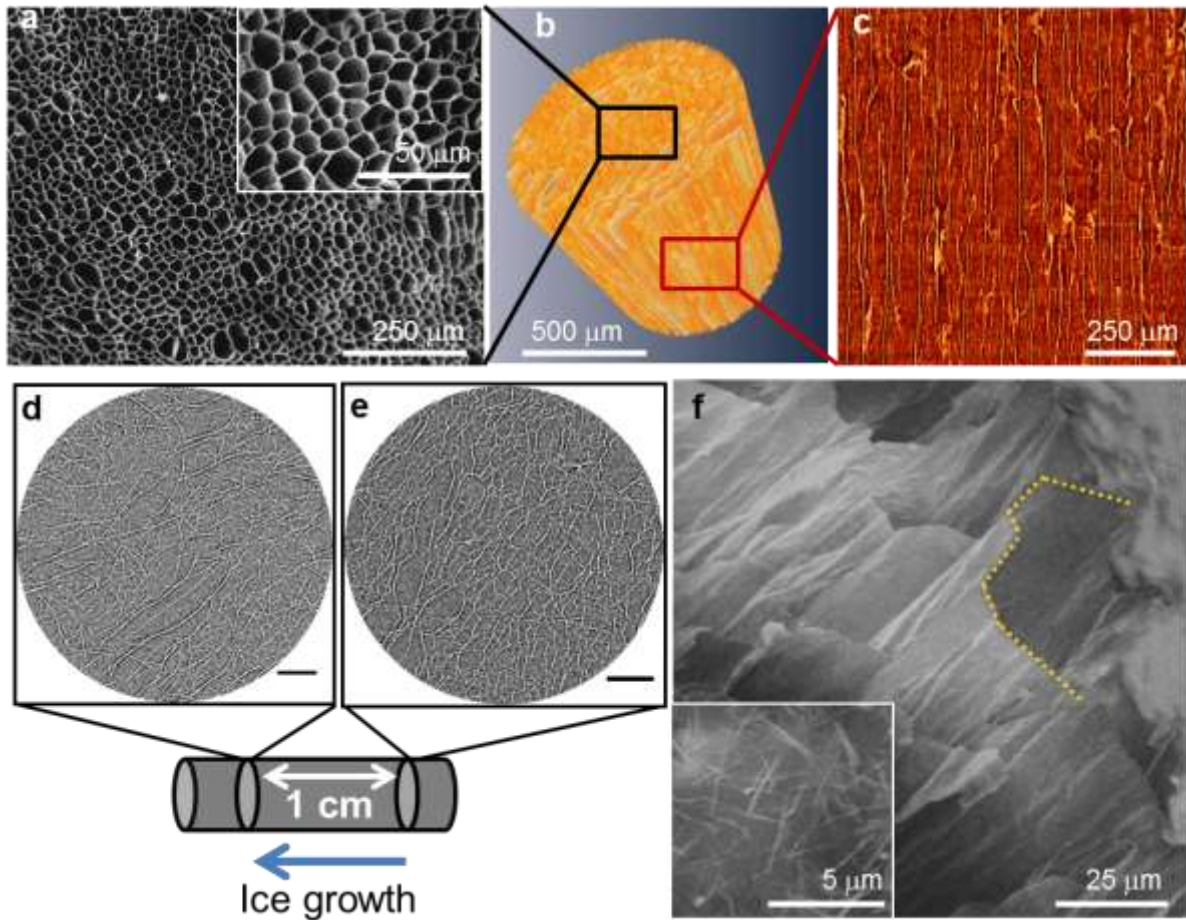


**Figure 2. Microstructure of freeze-cast nanocomposite foams.** **a)** Scanning electron microscopy (SEM) cross-section image of a freeze-cast nanocomposite foam that contain cellulose nanofibres (CNF), graphene oxide (GO), sepiolite (SEP) and boric acid (BA). **b)** A 3D reconstruction of the tubular pore structure of the nanocomposite foam derived from X-ray microtomography. **c)** An X-ray microtomography image showing that the tubular pores are straight and several millimetres long in a nanocomposite foam with a composition of 77 % CNF-10 % GO-10 % SEP-3 % BA (in wt.%). **d)** and **e)** are X-ray microtomography cross-sections of a nanocomposite foam taken at the upper and at the bottom part, respectively. Scale bars: (d, e) 100  $\mu\text{m}$ . **f)** High-resolution SEM image of a foam wall where the yellow dotted line indicates a section of the tubular cell. The inset shows distributed SEP nanorods within the cell wall. The nanomaterials are homogeneously distributed in the cell walls forming an anisotropic tubular pore structure as result of the unidirectional freeze-casting process.

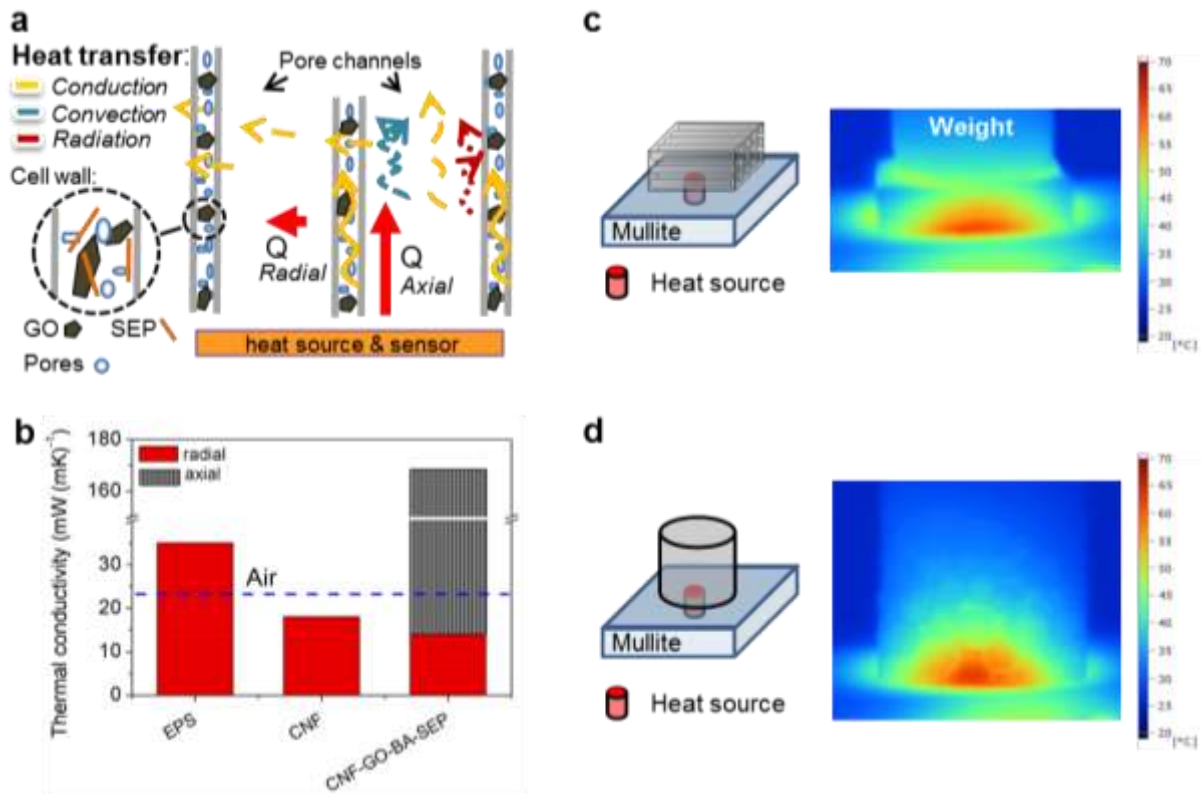


**Figure 3. Thermal transport properties of anisotropic nanocomposite foams. a)** Schematic illustration of contributions to thermal conductivity in radial and axial direction of a foam with oriented pores (not drawn to scale). **b)** Thermal conductivity values in axial and radial direction of cellulose nanofibre (CNF) and CNF-graphene oxide(GO)- boric acid(BA)-sepiolite(SEP) foams compared with expanded polystyrene (EPS). The thermal conductivity normal to the tubular pores is significantly lower than the value for air. **c)** Schematic (left) and thermographic (right) images of CNF-GO-BA-SEP nanocomposite foam with the tubular pores oriented normal to the heat source compared with **d)** a closed-cell EPS foam. The heated volume of the CNF-GO-BA-SEP nanocomposite foam is smaller and more homogeneous than the EPS foam. The colours in the thermographic images show the temperature distribution on the surface of the foams. The rectangular nanocomposite foam (c, right image) was pressed onto the heat source with a weight made of zirconia.



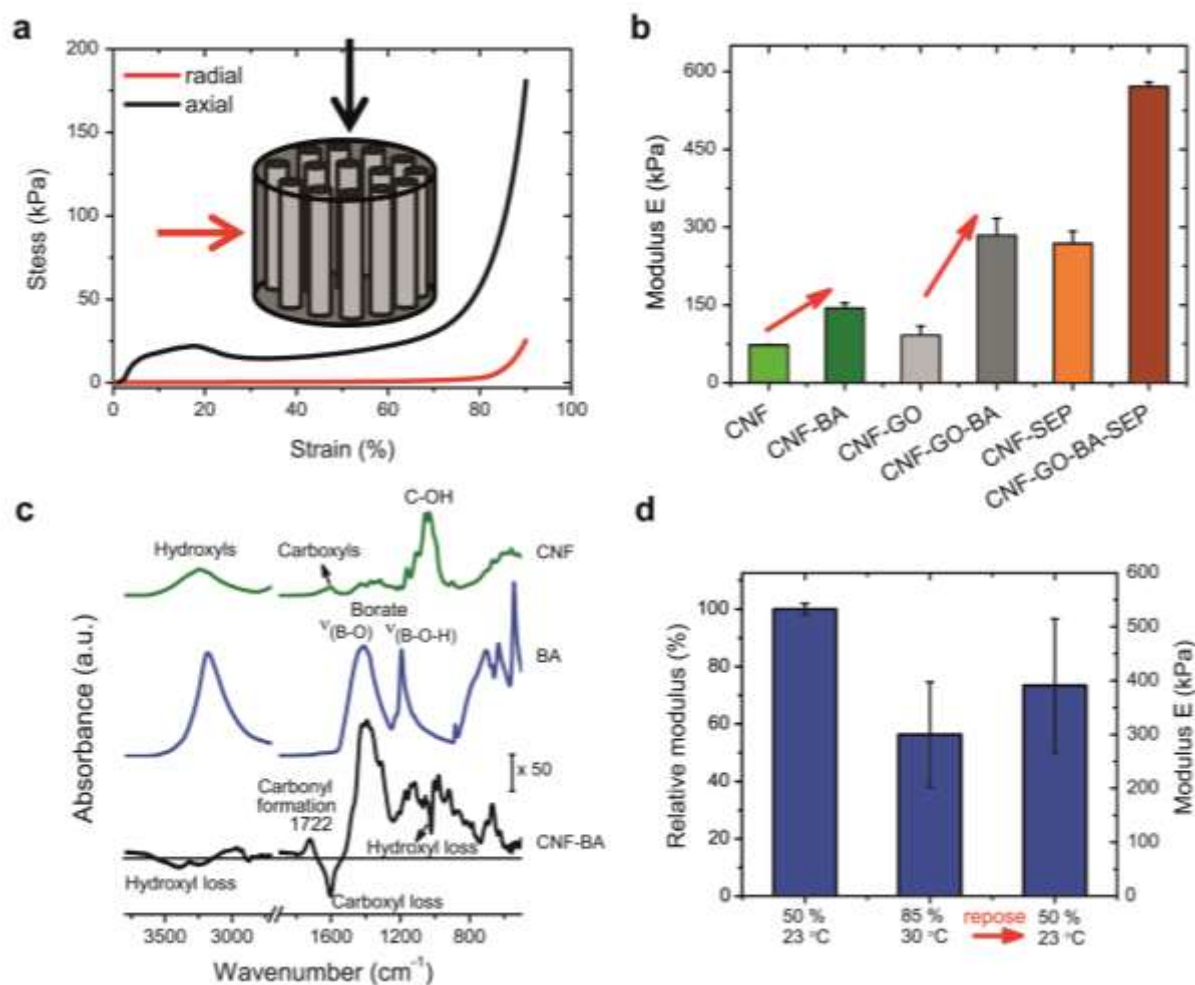


**Figure 4. Mechanical properties and cross-linking of nanocomposite foams.** **a)** Stress-strain measurements of a nanocomposite foam containing 77 % cellulose nanofibres (CNF), 10 % graphene oxide (GO), 10 % sepiolite (SEP), 3 % boric acid (BA) (in wt.%) determined in both the strong and stiff axial orientation and the much weaker radial orientation with respect to the tubular pores. **b)** Young's moduli,  $E$ , of the nanocomposite foams obtained from the elastic region of the compression tests. The red arrows highlight the increase in Young's modulus brought about by the addition of boric acid. **c)** IR spectra of cellulose nanofibres (CNF) boric acid (BA) and a differential spectrum of CNF-BA with respect to CNF. The spectra indicate that boric acid interacts with the hydroxyl and carboxyl groups of CNF. **d)** Young's moduli,  $E$ , of a nanocomposite foam before, during and after exposure to 85% relative humidity. The measurements show partial recovery of the mechanical properties after cycling in moist conditions.



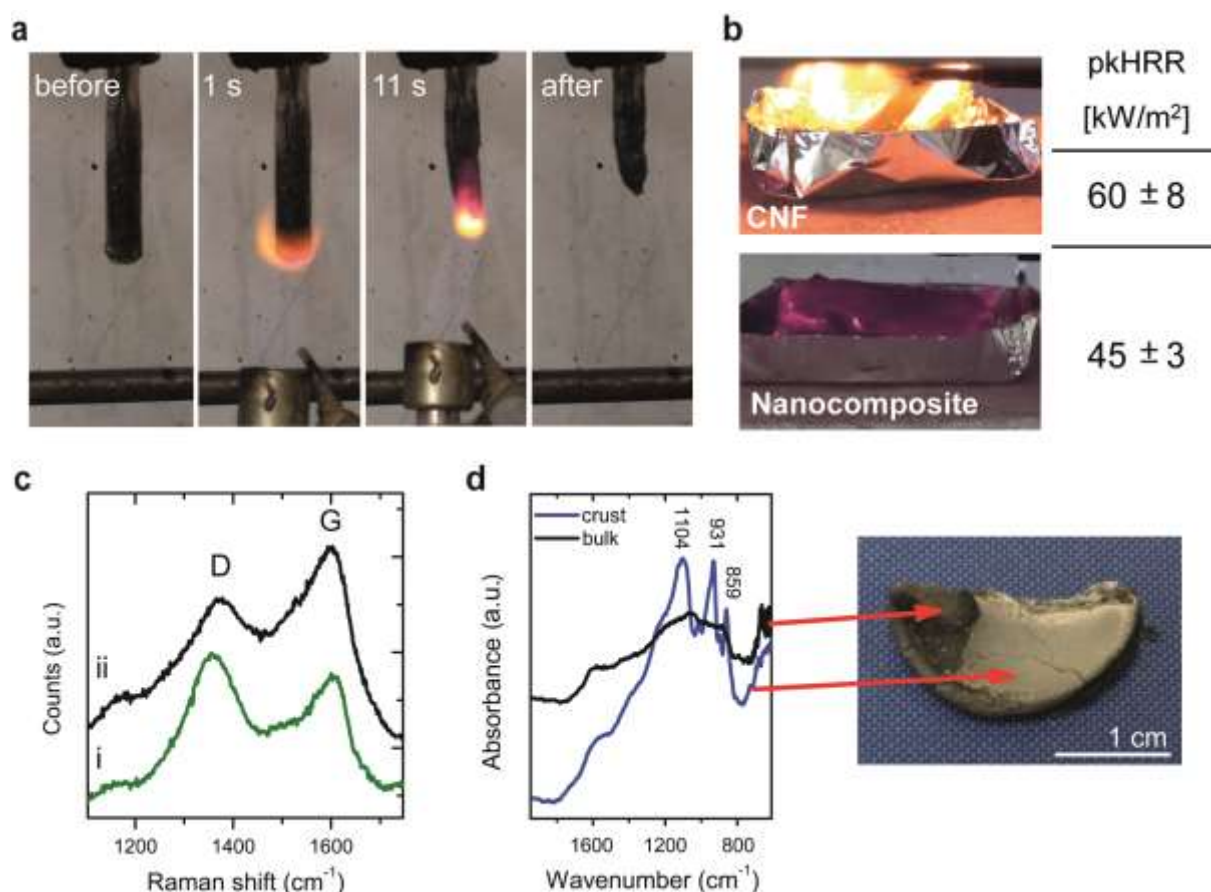


**Figure 5. Flame resistance of the nanocomposite foams.** **a)** Vertical burning test (UL94) of a nanocomposite foam containing 77 % cellulose nanofibres (CNF), 10 % graphene oxide (GO), 10 % sepiolite (SEP), 3 % boric acid (BA) (in wt.%). The panel shows the foam before the test, 11 s of application of a methane flame and the foam after the test showing high fire retardancy. **b)** Photos of CNF and CNF-GO-BA-SEP nanocomposite foams during the cone calorimetry test together with the corresponding peak of heat release rates (pkHRR). The test reveals high combustion resistance for the nanocomposite foam at the limit of non-ignitability while CNF foams are entirely combusted. **c)** Raman spectra of a CNF-GO-BA-SEP nanocomposite foam before (trace i) and after burning indicating boric acid mediated graphitization of nanocellulose (trace ii). **d)** IR spectra and the corresponding photo of a CNF-GO-BA-SEP foam after burning show a clay-rich crust and the bulk underneath. Both the graphitization and the formation of the protective crust contribute to the combustion resistance of the foams

**Table 1.** Microstructural properties of CNF and nanocomposite foams.

Foam composition	CNF	CNF-GO-BA-SEP
App. Density [a,b] ( $\text{kg m}^{-3}$ )	$5.6 \pm 0.2$	$7.5 \pm 0.2$
Porosity [c] (%)	99.6	99.5
2-dimensional pore density [d,b] ( $10^5 \text{ cm}^{-2}$ )	$5.2 \pm 0.1$	$2.9 \pm 0.4$
Feret diameter ( $\mu\text{m}$ ) [d,e]	18	22

[a] Apparent densities were calculated from the weight and volumes of the foams

[b] Given as the mean value followed by the standard deviation.

[c] The porosity is defined as  $(1 - \rho_{rel}) \cdot 100 \%$  where  $\rho_{rel}$  is the relative density. The relative density is calculated as  $\rho_{app}/\rho_{sc}$  where  $\rho_{sc}$  is the skeletal density. The skeletal density is estimated from a weighted average of the densities of the components using the following density values for: CNF =  $1460 \text{ kg m}^{-3}$ , GO =  $2200 \text{ kg m}^{-3}$ , SEP =  $2300 \text{ kg m}^{-3}$ , and BA =  $1440 \text{ kg m}^{-3}$ .

[d] Estimated from SEM image analysis of cross-sections of the foam.

[e] Median values obtained from cumulative histograms obtained by SEM image analysis.

## Acknowledgements

This work was supported in part by the Swedish strategic foundation (SSF) (grant RMA11-0065), the Wallenberg wood science centre (WWSC) and the Swedish Research Council (VR). LB also thanks the Humboldt foundation and B.W. and G.S.A thank the Cost Action MP1202 for support. L. Wågberg is thanked for providing the nanocellulose. We thank, L. Berglund, J. Kochumalayil, J. Yuan, D. Kocjan and Lagerwall for help and valuable discussions and Z. Bacsik, A. Ojuva, J. Hornatowska, P. Fajdiga, M. Vrabelj, A. Di Blasio and F. Cuttica for various contributions.

**Author contributions:**

B.W., G.S.A., L.B. and M.A. conceived the study and B.W. and L.B. planned and coordinated the work. A.K. performed the thermal conductivity measurements and analysed the data together with B.W. B.W. carried out and analysed the mechanical strength data. B.W., F.C. and G.C. carried out and analysed the flame retardancy measurements. B.W., G.S.A. and L.B. wrote the manuscript.

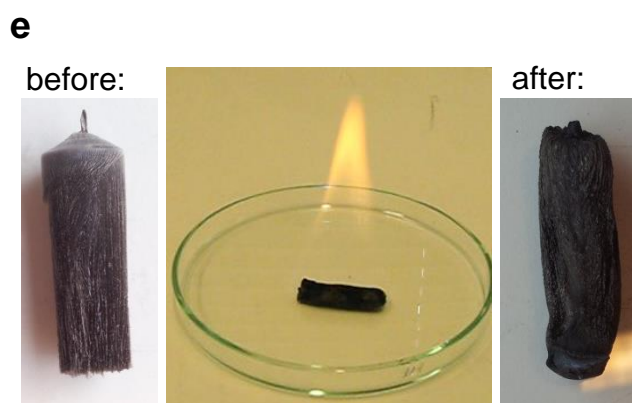
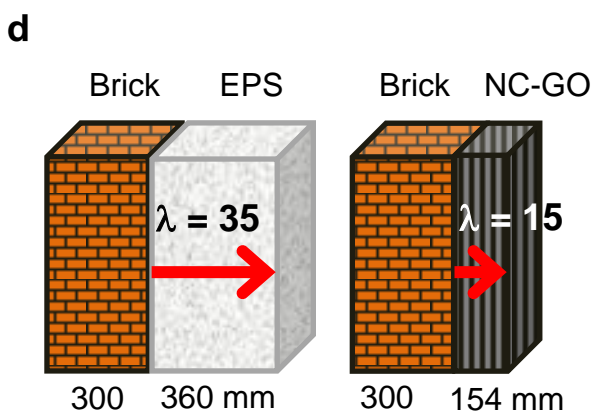
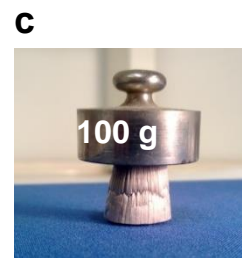
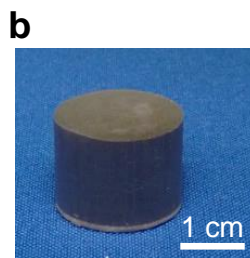
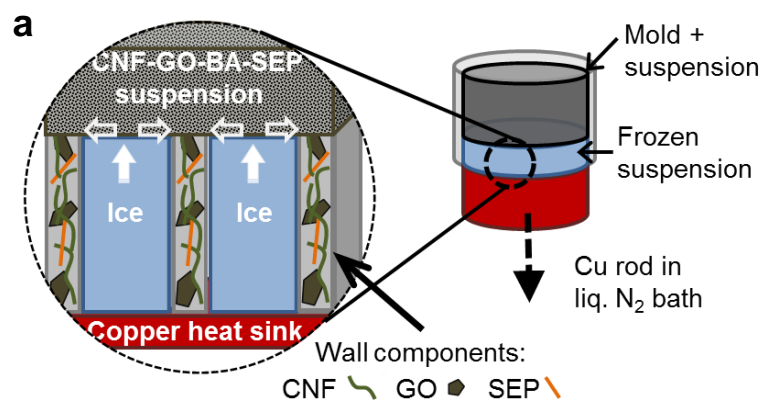
**Additional information**

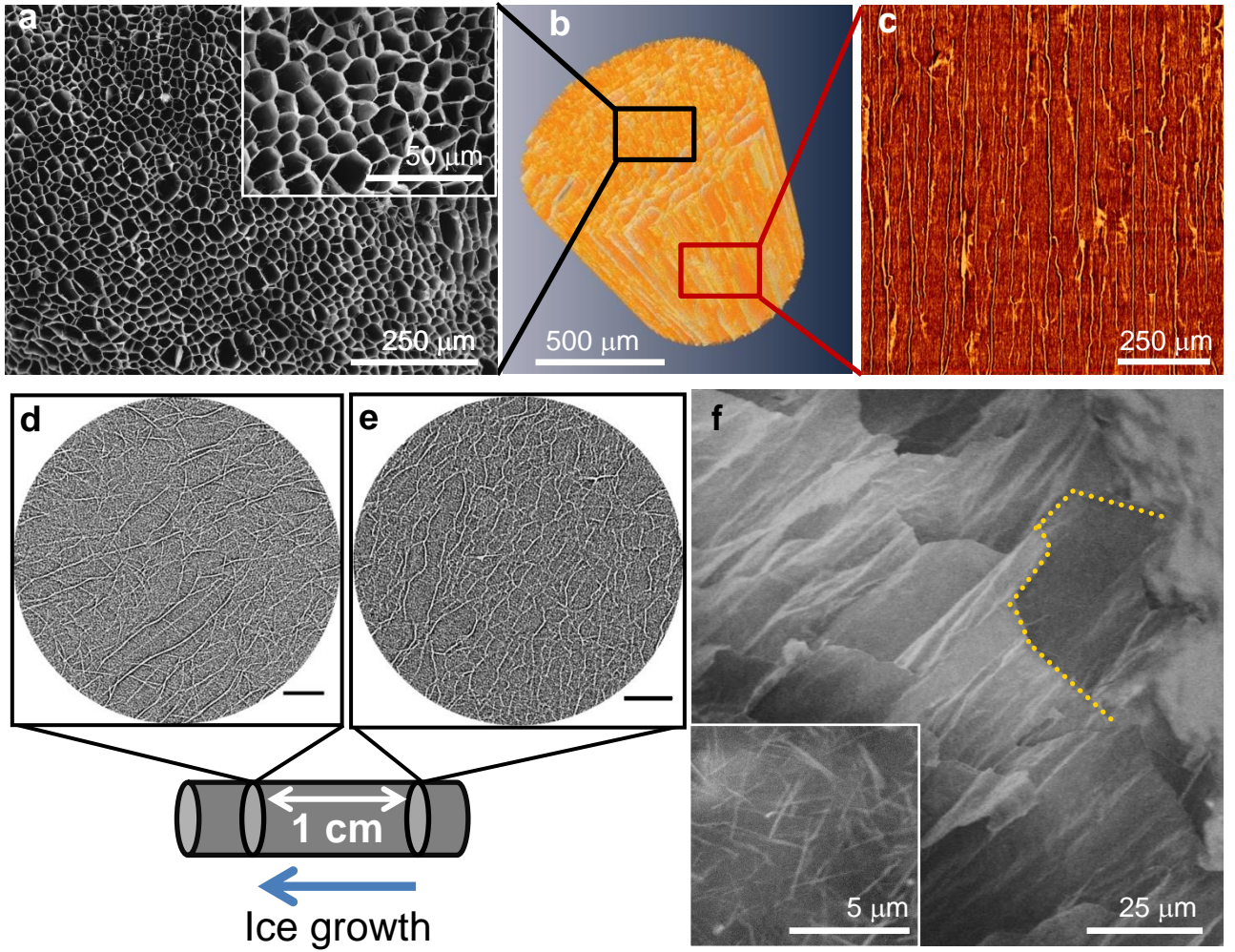
Supplementary information accompanies this paper at [www.nature.com/naturenanotechnology](http://www.nature.com/naturenanotechnology). Reprints and permission information is available online at <http://npg.nature.com/reprintsandpermissions/>. Correspondence and requests for materials should be addressed to L.B.

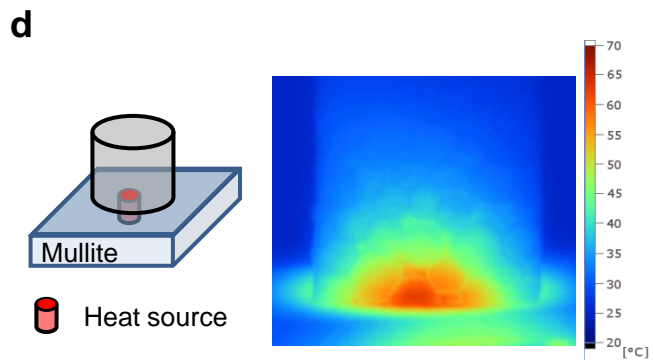
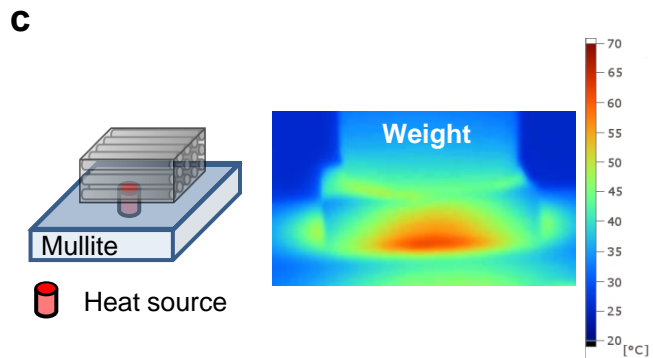
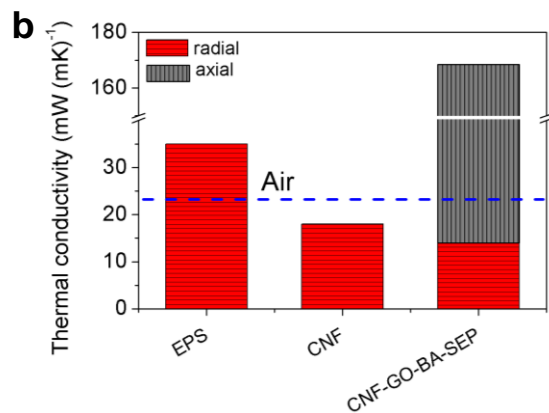
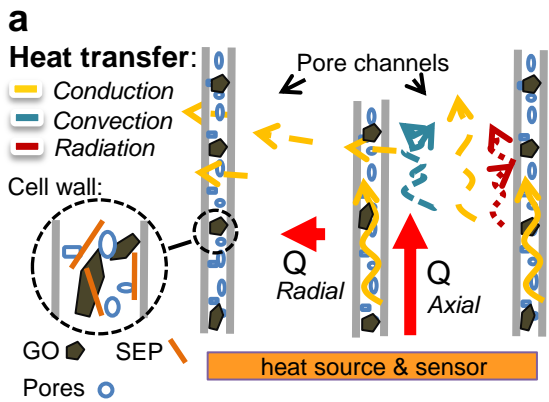
**Competing financial interests**

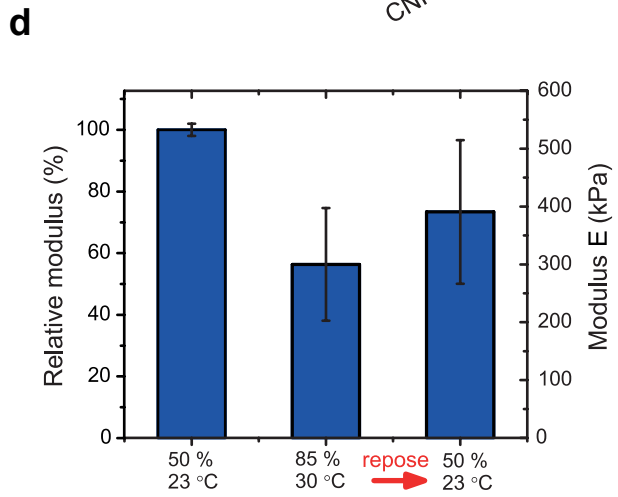
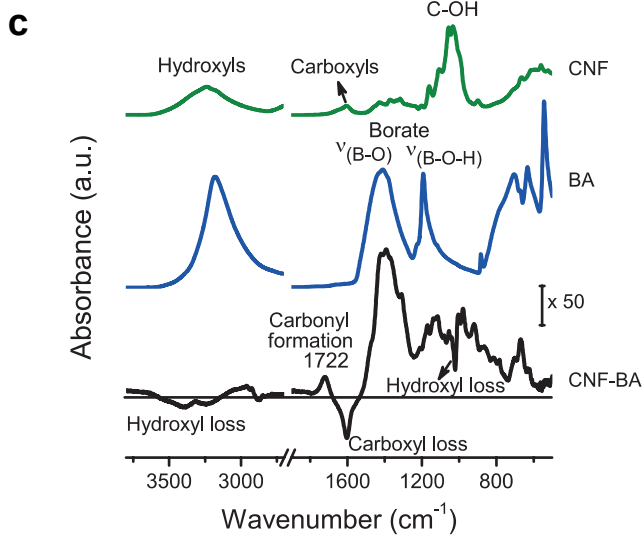
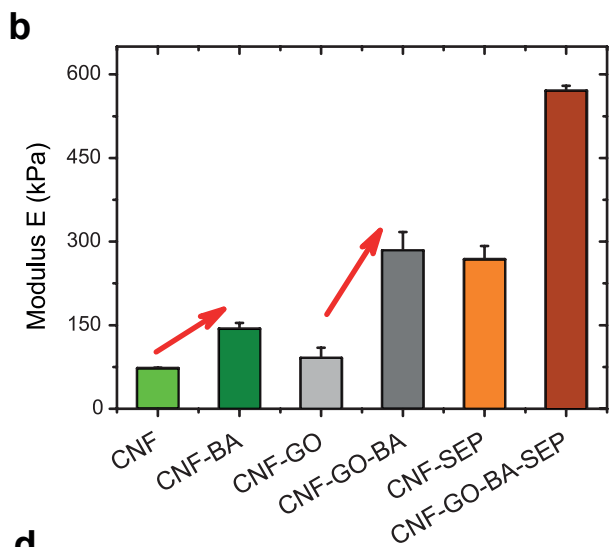
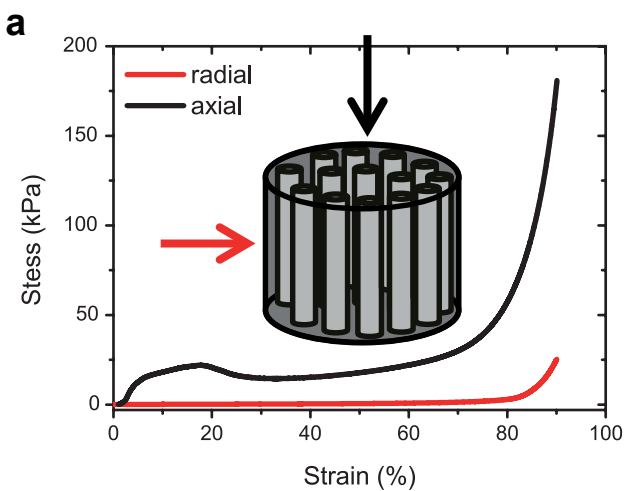
The authors declare no competing interests

**Keywords:** thermal conductivity, flame retardancy, nanocellulose, graphene oxide, clay, strength, foams, freeze-casting.











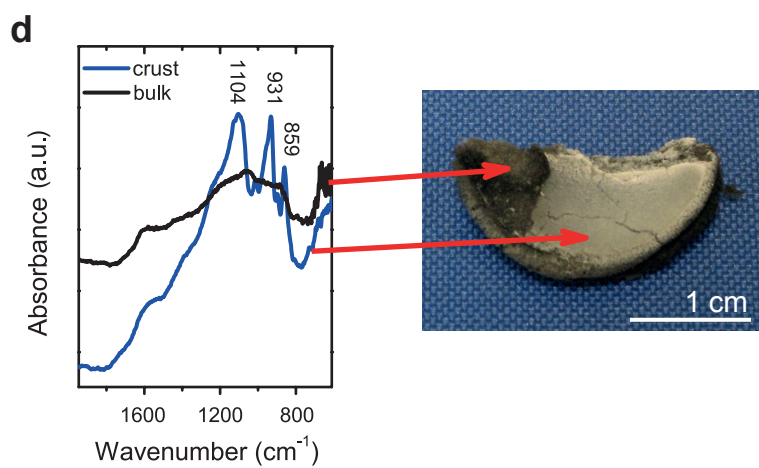
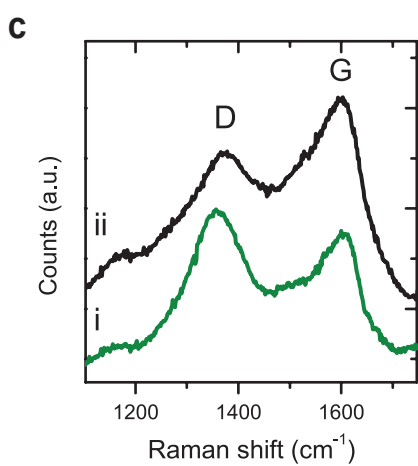
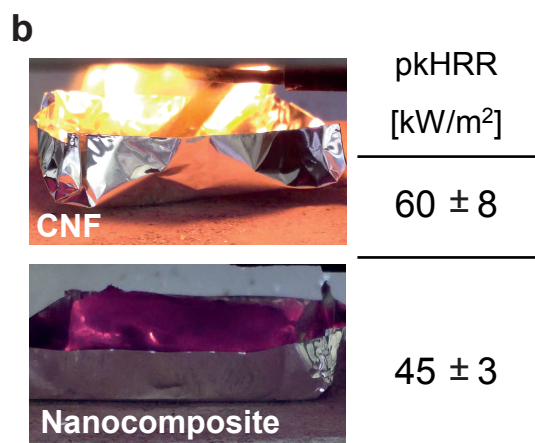
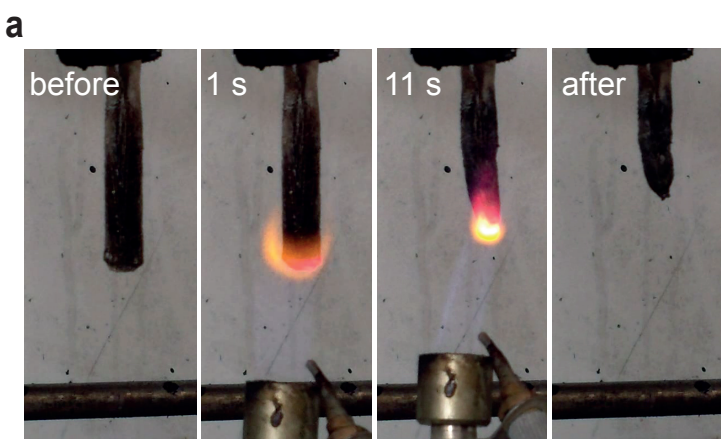




**Table 1.** Microstructural properties of foams.

<b>Foam composition</b>	<b>CNF</b>	<b>CNF-GO-BA-SEP</b>
App. Density [a,b] (kg m <sup>-3</sup> )	5.6 ± 0.2	7.5 ± 0.2
Porosity [c] (%)	99.6	99.5
2-dimensional pore density [d,b] (10 <sup>5</sup> cm <sup>-2</sup> )	5.2 ± 0.1	2.9 ± 0.4
Feret diameter (μm) [d,e]	18	22

[a] Apparent densities were calculated from the weight and volumes of the foams

[b] Given as the mean value followed by the standard deviation.

[c] The porosity is defined as  $(1 - \rho_{rel}) \cdot 100 \%$  where  $\rho_{rel}$  is the relative density. The relative density is calculated as  $\rho_{app}/\rho_{sc}$  where  $\rho_{sc}$  is the skeletal density. The skeletal density is estimated from a weighted average of the densities of the components using the following density values for: CNF = 1460 kg m<sup>-3</sup>, GO= 2200 kg m<sup>-3</sup>, SEP= 2300 kg m<sup>-3</sup>, and BA = 1440 kg m<sup>-3</sup>.

[d] Estimated from SEM image analysis of cross-sections of the foam.

[e] Median values obtained from cumulative histograms obtained by SEM image analysis.